

A three-dimensional fluid-controlled earthquake model: Behavior and implications

Stephen A. Miller

Geology Institute, ETH-Zürich, Switzerland

Yehuda Ben-Zion

Department of Earth Sciences, University of Southern California, Los Angeles

Jean-Pierre Burg

Geology Institute, ETH-Zürich, Switzerland

Abstract. We describe the behavior of a three-dimensional, fluid-controlled fault model that couples the dominant mechanical effects of fluid within a cellular fault zone with shear stress accumulation from constant plate motion applied at the downward continuation of the fault. Improvements from a previous model include long-term plate motion loading and porosity creation through dilatant slip, which allow the model to evolve to its steady state dynamic equilibrium. The examined results include slip and slip-deficit accumulation, pore pressure buildup and release, stress states, the emergence of seismic scaling relationships, and frequency-size statistics of model earthquakes. We find that asperities develop naturally within the model, reflecting the disorganization of the evolving stress state in Mohr space. The dynamical interaction of shear stress and effective normal stress perturbs the initial uniform stress state to a complex state that produces transient asperity development along the fault. These “Mohr-space” asperities spontaneously evolve, disintegrate, reemerge, and migrate along the fault plane. The general model behavior is independent of the state of the fluid pressure. In four examined cases, which span the range of possible fault zone overpressures, the equilibrium condition is that which occupies all of the available Mohr space. Maximum slip deficits along the fault depend on the degree of fault weakness, ranging from about 3 m for a weak fault to over 30 m for a strong fault after 4000 years of model evolution. For events that breach the surface the seismic moment scales with the cube of the source dimension $M_o \sim L^3$, which reflects the slipped area times the depth extent of the rupture. This scaling crosses isolines of stress drop. For confined events, $M_o \sim L^2$ along isolines of stress drop, but no general scaling emerges. Clusters emerge between stress drop versus seismic moment and stress drop versus source dimension, with large events converging to average stress drops of about 8 MPa for a weak fault and about 20 MPa for a strong fault.

1. Introduction

Advances in earthquake prediction, seismic hazard assessment, and interpretations of seismicity and surface deformation data are impeded by the lack of a general, mechanistic model capturing the dominant processes controlling seismicity and faulting. The principal problem in earthquake source mechanics is an appropriate reconciliation between two fundamental observations. First, many major faults slip under low shear stress [Zoback and Beroza, 1993], and second, a large degree of fault zone heterogeneity is required to obtain the observed wide range of event sizes and other manifestations of seismic complexity [Ben-Zion and Rice, 1993].

Contemporary models of earthquakes and faulting often focus on either stress transfer, high pore pressures, or means of

generating complexity. Stress transfer models [Harris, 1998] calculate the change in Coulomb failure stress along faults at defined locations and orientations relative to the site of a large earthquake in order to determine changes in seismic hazard. An advantage of these models is their simplicity and the fact that simple elasticity theory represents an appropriate approximation to upper crustal faulting [Reasenberg and Simpson, 1992; King et al., 1994; Harris and Simpson, 1996; Deng and Sykes, 1997; Stein et al., 1997]. Model results are often presented in “map view,” with general approximations to processes occurring at depth, and use an “effective” friction coefficient to account for pore pressure effects. Best fits to the data require effective friction coefficients of around 0.1–0.4, indicative of mildly overpressured faults [Robinson and Benites, 1995; Harris and Simpson, 1996].

Models based on high pore pressures are motivated by evidence from a variety of sources indicating that high pore pressures within fault zones may contribute to the seismic process and may be responsible for fault weakness. The weak fault requirement derives from several lines of evidence, including low heat flow [Lachenbruch and Sass, 1980; Sass et al., 1998], stress

measurements [Zoback, 1987], and numerical modeling [Zhong and Gurnis, 1996]. The possible mechanical effects of fluids on faulting are known [Sibson, 1973], and fluid overpressure as a mechanism for fault weakness has gained significant attention [Hickman et al., 1995]. Relevant models focus on mechanisms for generating and maintaining fluid pressures in excess of hydrostatic [Walder and Nur, 1984]. Creep compaction as a mechanism for generating high fluid pressures, based on a similar mechanism observed in the laboratory [Blanpied et al., 1992], has led to models of this phenomenon [Sleep and Blanpied, 1992; Lockner and Byerlee, 1995; Segall and Rice, 1995; Miller et al., 1996; Henderson and Maillot, 1997; Yamashita, 1998]. Fluid sources at depth have also been considered as a mechanism for elevated pore pressures [Rice, 1992], and modeling of porosity waves provides theoretical support for localized zones of high pore pressures [Connolly, 1997; Connolly and Podladchikov, 1998]. Compartmentalized high fluid pressures [Byerlee, 1990, Byerlee, 1993; Miller et al., 1996], suggested to exist in fault zones, are supported in part by seismic and drilling experiments along a décollement near Barbados [Moore et al., 1995; Fisher and Zwart, 1996].

However, high fluid pressures alone can not generate a wide range of earthquake sizes associated with the Gutenberg-Richter relationship [Kanamori and Anderson, 1975], and do not produce the heterogeneity necessary for seismic complexity [Nur, 1978; Das and Kostrov, 1988; Bak and Tang, 1989; Ben-Zion and Rice, 1993, 1995; Boatwright and Cocco, 1996; Cochard and Madariaga, 1996; Shaw, 1997]. Complexity is easily generated by models of self-organized criticality (SOC) and simulations employing spring-mass systems [Bak and Tang, 1989; Carlson and Langer, 1989; Main, 1996; Heimpel, 1997]. Modeling earthquakes as an SOC system may provide an approximate framework for understanding complex dynamics, and it produces power law statistics. This is attractive since power law statistics are abundant in nature and reflect a self-similar generating mechanism. These models are however, limited because they typically lack physical processes to drive the system or a length scale to compare specific observations beyond general power law statistics of model results.

For additional progress, the following questions must be addressed. First, if nature and earthquakes are self-organizing systems [Bak and Tang, 1989], what are the physical and/or chemical processes controlling the organization? Second, how can we go beyond vague power law statistics to make comparisons with other multidisciplinary observations that provide more

stringent testing of hypotheses and models? If a model can be found to match spatial and temporal observations on many scales (and with the proper units), then such a model can be used to extract potential precursory phenomena based on physical processes, thus allowing for testable predictions given adequate data.

The objective of this paper is to reexamine the earthquake process as a coupled dynamical system in which fluids play a dominant role in its evolution. We propose that the direct coupling between plate motion loading and fluid-controlled processes conditions faults repeatedly for the occurrence of large earthquake ruptures. We describe the behavior of a three-dimensional earthquake model that couples a cellular automaton model of fluid flow with large-scale structure and elastic dislocation theory. The model is deterministic, physically simple, and inherently discrete in the sense of Rice [1993] and Ben-Zion and Rice [1995]. This work generalizes a previous model [Miller, 1996; Miller et al., 1996; Miller, 1997] and produces realistic complexity, self-organization, and correct physical units. The three-dimensional model creates spatiotemporal property variations, while elasticity and the assumed large-scale structure allow direct comparisons with detailed observations.

The paper is arranged as follows. In sections 2 and 3, we describe the model with emphasis on improvements made since a previous version [Miller et al., 1996]. Some general results are then presented to introduce this dynamical system of fluid pressure and shear stress. Results from the range of possible overpressure states demonstrate that the general behavior of the model is independent of the initial conditions. We explore the range of potential fluid pressure regimes, from highly overpressured faults to normally pressured faults. We examine the evolved stress states, fluid pressure, slip deficit, seismic potential, porosity, and seismic scaling relationships.

2. The Conceptual Model

The model is conceptually and numerically simple. The fault (Figure 1) contains a matrix of computational cells representing discrete fluid pressure compartments in a deforming elastic solid. Fault compaction increases fluid pressure in these compartments by either a porosity reduction mechanism [Walder and Nur, 1984; Gavrilenko and Gueguen, 1993; Hickman and Evans, 1995] or a fluid source [Rice, 1992; Wong et al., 1997]. Plate motion increases the shear stress along the fault plane. For any cell, shear stress accumulation and increasing fluid pressure will eventually

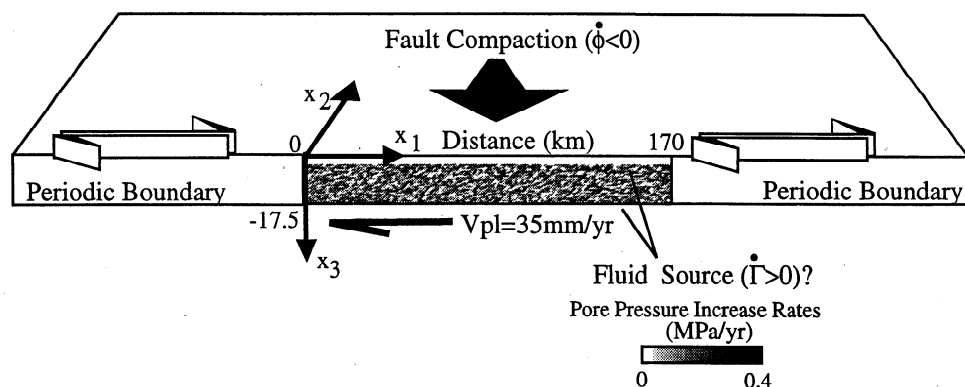


Figure 1. Model of a right-lateral strike-slip fault in a three-dimensional elastic half-space and bounded by periodic repeats of the same fault along strike. It measures 170 km along strike and 17.5 km in depth and is coupled to a viscous substrate moving at a plate velocity of 35 mm/yr. The model is subjected to pore pressure increases from fault compaction or a fluid source and from shear stress accumulation from plate motion.

bring the cell to brittle failure. At failure, (1) shear stress is reduced on the cell by a stress drop related to slip via elastic dislocation theory [Chinnery, 1963; Stuart et al., 1985; Stuart, 1986; Rice, 1993], and (2) dilatant slip increases the local permeability and allows pressure equilibration of neighbor cells. The effect of a slip event is to increase shear stress on all other cells in the fault zone, while simultaneously changing the fluid pressure state, either in the failing cell and surrounding region or in much of the fault zone when many cells are involved. The reduction in shear stress and increase in effective normal stress due to slip thus heal the failed cell, while the stress and fluid transfer to neighbor cells bring them closer to failure. Considering all the cells in the matrix, each following its own path, the complex interplay between shear stress redistribution and evolving zones of high pore pressure self-organize into regions of varying degrees of shear stress and overpressure. Regions can also arise that have avoided the evolving permeability network, and these hydraulically isolated zones can absorb significant shear stresses from the failure of other cells in the matrix. We will show that in Mohr-space this dynamical system is intractable on the local scale but achieves a steady state condition with well-defined emerging macroscopic behaviors.

We consider a vertical strike-slip fault in a three-dimensional elastic (Poisson solid) half-space. The model fault extends from $0 \leq \text{fault} \leq 170\text{km}$, with periodic repeats of the same fault along strike [Rice, 1993]. Periodic repeats of the same fault along strike approximate an infinite fault. The fault extends to a depth of 17.5 km and is coupled to a ductile substrate moving at a constant plate velocity of 35 mm/yr. Although the fault dimensions were initially chosen to represent the central San Andreas Fault (SAF), the model used here is general in that no assumptions are made regarding creeping sections, locked sections, or other specific behaviors. The model is applicable to any strike-slip partitioned transpressional system. Strike-slip partitioning provides components of increased shear stress from plate motion and increased pore pressures from fault compaction. For the SAF, fault normal motion is indicated by the geomorphology of the region and measurements of nonzero fault normal strain rates [Harris and Segall, 1987]. A fold and thrust belt striking subparallel to the central SAF along its length [Stein and Ekström, 1992] provides evidence for large-scale fault normal contraction and a compacting environment to the strike-slip fault zone. In addition to fault compaction, other possible fluid sources include dehydration of hydrous minerals associated with the Franciscan complex [Wallace, 1990], channeling of fluids from below by the subducting Pacific plate [Braun and Beaumont, 1995], or precipitation/dissolution processes [Hickman and Evans, 1995]. In the present work we focus on transpressional environments, but we suggest the model may also have application to transtensional regimes and shallow-intermediate subduction zone seismicity.

We investigated model realizations with different grid sizes. In the highest-resolution model the fault plane consisted of 40,000 discrete cells, with 400 along strike and 100 through the depth. Such high resolutions are computationally cumbersome, so most of the results presented here are from models of 128 x 32 cells or 256 x 64 cells. We note that the results and implications discussed in this paper do not depend on the model resolution. High-resolution calculations are beneficial for extending the range of possible event sizes, but the overall behavior is independent of the resolution.

Major drawbacks of a previous model [Miller, 1996; Miller et al., 1996] included the simplifying assumptions regarding shear stress accumulation and the lack of a mechanism for creating

porosity associated with slip events. Here, shear stress accumulation from plate motion, as in the models of Rice [1993] and Ben-Zion and Rice [1993], is included. The porosity production formalism developed by Sleep [1995], based on experimental results of Marone et al. [1990], was also incorporated into the model. These improvements allow the model to simulate features emerging over many earthquake cycles because it accounts for both porosity creation and destruction. In the previous model, porosity lost through compaction was not recoverable.

3. The Numerical Model

3.1. Plate Motion

Following Rice [1993] and Ben-Zion and Rice [1995], a constant plate velocity of 35 mm/yr is imposed at the downward continuation of the model fault. The increase in shear stress along the model fault is

$$\tau_i = \frac{G}{2\pi} \sum_{j=1}^N k_{ij} (\delta_j - V_{pl}(t)) \quad (1a)$$

where τ_i is the shear stress on cell i related to the displacement of the plate $u = V_{pl}(t)$ relative to slip δ_j , on all cells j through the stiffness matrix (k_{ij}). The stiffness matrix was calculated assuming 10 periodic repetitions of the fault along strike [Rice, 1993]. The failure condition is a simple cohesionless friction with a friction coefficient of 0.6, and the shear modulus G is taken as 30 GPa. Time steps in the model are controlled by the minimum time required to fail one, and only one, cell. This ensures that all events are triggered by one hypocenter. Average time steps are about 10–20 days but can range from a day to several months.

When a cell reaches the failure condition and slips, the shear stress on that cell drops by 80% of the preslip shear stress. This assumed stress drop is arbitrary, but it has the effect of a total stress drop model. The effects on the model behavior using other assumed stress drops and friction coefficients are addressed in section 4.1. At slip, the reduction in the τ_{21} component of the stress tensor is redistributed to all locations in the elastic half-space by [Chinnery, 1963; Stuart et al., 1985; Stuart, 1986; Okada, 1992; Rice, 1993; Ben-Zion and Rice, 1995; Miller et al., 1996]

$$\tau_i = \frac{G}{2\pi} \sum_{j=1}^N k_{ij} \delta_j \quad (1b)$$

The additional shear stress on cell i from a slip event on cell j may induce failure on cell i , and the shear stress is redistributed within the fault plane until the stress state of all cells is below the failure condition.

3.2. Porosity Reduction and Porosity Production

While shear stress accumulates from plate motion, pore pressures increase from fault compaction. The rate of pore pressure increase in an impermeable region is

$$\left. \frac{\partial P_f}{\partial t} \right|_{\text{noflow}} = \frac{\dot{F} - \dot{\phi}_{\text{plastic}}}{\phi(\beta_\phi + \beta_f)} \quad (2)$$

where $\dot{F} - \dot{\phi}_{\text{plastic}}$ is a source term providing fluid pressure through porosity reduction ($-\dot{\phi}$) or a direct fluid source (\dot{F}), ϕ is porosity and β_ϕ and β_f are the pore and fluid compressibility,

respectively [Segall and Rice, 1995; Wong et al., 1997]. Equation (2) is the only parameter that varied in the results presented.

It has been shown experimentally [Marone et al., 1990] and used in other models [Sibson, 1973, 1992; Lockner and Byerlee, 1994; Segall and Rice, 1995; Sleep, 1995] that dilatancy accompanies slip, decreasing pore pressure and increasing the effective stress (dilatancy hardening). Following Sleep [1995] and Marone et al. [1990], a certain fraction of energy from frictional sliding is used to create new crack porosity that accompanies slip. In terms of slip displacement, this can be written by modifying results from Sleep [1995] as

$$\frac{\partial \phi}{\partial \delta} = \frac{\beta_m (\phi_m - \phi) \mu}{W \phi_m} \quad (3)$$

where ϕ is the porosity created with slip δ , β_m is the fraction of energy that goes into new crack creation, ϕ_m is the saturation porosity which limits the amount of crack porosity that can be created, μ is the friction coefficient, and W is the fault width. The values for β_m , ϕ_m and W were taken from Sleep [1995] and were constant for all simulations. Since porosity is both created and destroyed, the rate of pore pressure buildup (equation 2) is an evolutionary parameter and is updated continuously in the numerical algorithm.

In this simple model we ignore pore pressure changes due to poroelastic stressing in the three-dimensional body. That is, pore pressure changes are due only to fault compaction, dilatant slip, and hydraulic communication with other regions along the fault at different fluid pressures.

3.3. Pore Pressure Redistribution

Pore pressure is modeled as a cellular automata, with permeability treated as a toggle switch (S.A. Miller and A. Nur, manuscript in preparation). That is, when a cell is below the failure condition, the permeability is zero. When a cell slips, we assume that permeability is infinite to the nearest neighbor cells. After a slip event the permeability is again approximated as zero. At slip the seal perpendicular to the fault strike remains intact, but the seal along strike is punctured and pore pressure in the failed cell equilibrates with the four nearest neighbor cells (sides, above, and below). This model roughly approximates qualitative explanations for observations of many exhumed fault zones [Caine et al., 1996]. Caine et al. [1996, p.1025] describe a fault zone architecture as consisting of a low-permeability core, a high permeability damage zone, and a low permeability protolith. For the core, they note that "the core may act as a conduit during deformation and as a barrier when open pore space is filled by mineral precipitation following deformation". Caine et al. [1996, p. 1028] describe the Dixie Valley fault zone and a fault zone in Greenland as examples where "the fault core acted as a short-lived, syndeformational, fluid flow conduit that then rapidly sealed to form a barrier to flow."

When a cell or cells slip, the neighboring cells are identified, and the pore pressure is redistributed among affected cells by conserving fluid mass and satisfying hydrostatic pore pressure gradients (after failure) within the hydraulically connected cells. The equilibrium fluid pressure among communicating cells is

$$\bar{P} = \frac{\sum_{i=1}^M (\varphi \beta)_i (P_i - pg \Delta h)}{\sum_{i=1}^M (\varphi \beta)_i} + pg \Delta h \quad (4)$$

where \bar{P} is the post failure pore pressure in the affected cells, P_i is the prefailure pore pressure, $(\varphi \beta)_i$ is the storage capacity of each cell ($\beta = \beta_\phi + \beta_f$), ρ is the fluid density, and the sum extends over affected cells M . The term Δh is measured from the depth of the slipped source cell, so a negative sign accompanies the shallower cells.

The numerical algorithm is as follows: (1) determine time step by searching for the minimum time necessary to initiate slip in one cell, (2) calculate shear stress increase from plate motion (equation 1a), (3) calculate pore pressure increase (equation 2), (4) redistribute shear stress (equation 1b), (5) calculate porosity from dilatant slip (equation 3), (6) redistribute pore pressures (equation 4), (7) search grid for induced slip, and (8) cycle model until all cells are below the failure condition. Repeat step 1. In the event that different parts of the computational matrix are slipping, the permeability network associated with a slipping region are identified and isolated from other evolving networks.

In the numerical algorithm, dilatancy only occurs when slip on a cell has taken place. When a cell slips, the amount of porosity created is then part of the total porosity used for the calculation of pore pressures (equation 4). If the neighbor cells have lower fluid pressure than the cell that failed, then the equilibrium pressure of affected cells may be greater than that before fluid communication occurred. In this case, the neighboring cells would be closer to failure (both from stress transfer and higher pore pressures), and the slip event may aid propagation of the event. On the other hand, if the neighbor cells are at a higher pressure than the cell that failed, fluid communication with the slipped cell would lower the fluid pressure of nearby cells, thus bringing them further from failure (quenching). Therefore both quenching and aiding a slip event are possible conditions within the model. An in-depth study of individual rupture events is necessary to determine how this aspect of the model affects the results.

4. Model Results

4.1. A Dynamical System in Mohr Space

The model is a feedback loop of increased shear stress from plate motion and failure of other cells, increased fluid pressure from fault compaction or another fluid source (including failures of neighboring cells), and decreased local shear stress and fluid pressure when a cell slips. The result is a dynamical system in Mohr space (shear stress versus effective normal stress) since all cells reside in this space (constrained by the failure condition) but are free to move along any path. A cell can approach the failure condition by a reduction in effective stress, an increase in shear stress from plate motion, or a combination of these mechanisms. Typical stress paths are shown for three cells along the center of the computational matrix, at depths of 4, 8, and 12 km (Figure 2). It is not very informative to track such complicated paths, but we can learn from the collective system behavior by examining the stress state evolution in Mohr-space (Figure 3). The stress state in Mohr space evolves from a uniform initial condition (Figure 3a), through transitory phase (Figures 3b-c), to a state where all possible stress states exist (Figures 3d-h). The disorder in stress space is maintained and is therefore the dynamic equilibrium state of this model (Figure 3i). The system is not fully self-organized until the entire space, bounded by the failure condition, is occupied. The emergence of the self-organized state is a general behavior of the model and will be shown to be independent of model input. As mentioned above, assuming a stress drop other

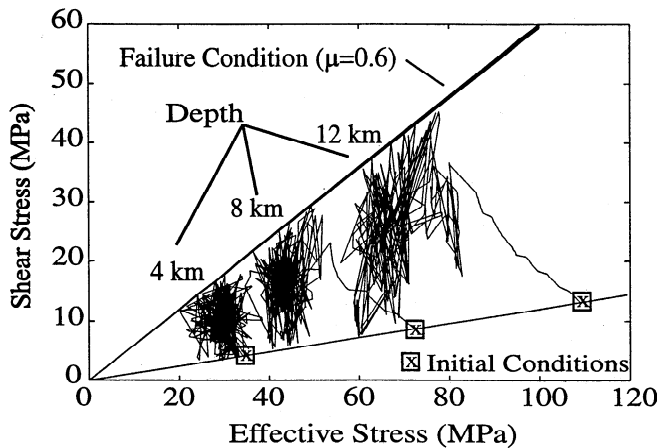


Figure 2. Typical stress paths of three cells in the center of the computational matrix at depths of 4, 8, and 12 km. Each cell is free to travel any route within this space but is confined by a simple friction failure condition. The paths are shown to demonstrate how the complex stress state in Mohr space (Figure 3) is established.

than 80% or a friction coefficient other than 0.6 does not affect the system behavior because it still finds the highest degree of disorder. A different assumed stress drop or friction coefficient merely limits the available stress space.

A simple analogy to the evolution in stress space is the thermodynamic example of two gasses in isolated compartments, separated by a plate. When the plate is removed, the particles interact randomly until kinetic equilibrium is attained at the state of highest entropy. The Mohr-space analogy holds because the system seeks a high degree of disorder, and this maximum disorder in stress space defines the self-organized dynamic equilibrium of the system. The associated evolution of stress states leads to spontaneous creation and destruction of asperities along the fault plane.

4.2. Model Input

One purpose of this work is to demonstrate how complexity develops from simplicity. In keeping with this, we reduced the model-input parameters to one variable; the initial distribution of pore pressure increase rates (equation 2). All other parameters are held constant. These are (1) constant plate velocity of 35 mm/yr, (2) simple friction with $\mu=0.6$, (3) an initial shear stress distribution set arbitrarily at 1 MPa/km, (4) a mildly overpressured fault with $\lambda=0.7$, and (5) a stress drop of 80% of the preslip shear stress. The parameter λ is defined as the ratio of pore pressure to lithostatic pressure and ranges from about 0.4 for hydrostatic pore pressures to 1.0 for lithostatic pore pressure.

We considered a range of pore pressure increase rates and initial distributions (Figure 4). These parameters, although not well constrained for active fault zones, were chosen to represent a physically reasonable range of possibilities, and that span a range

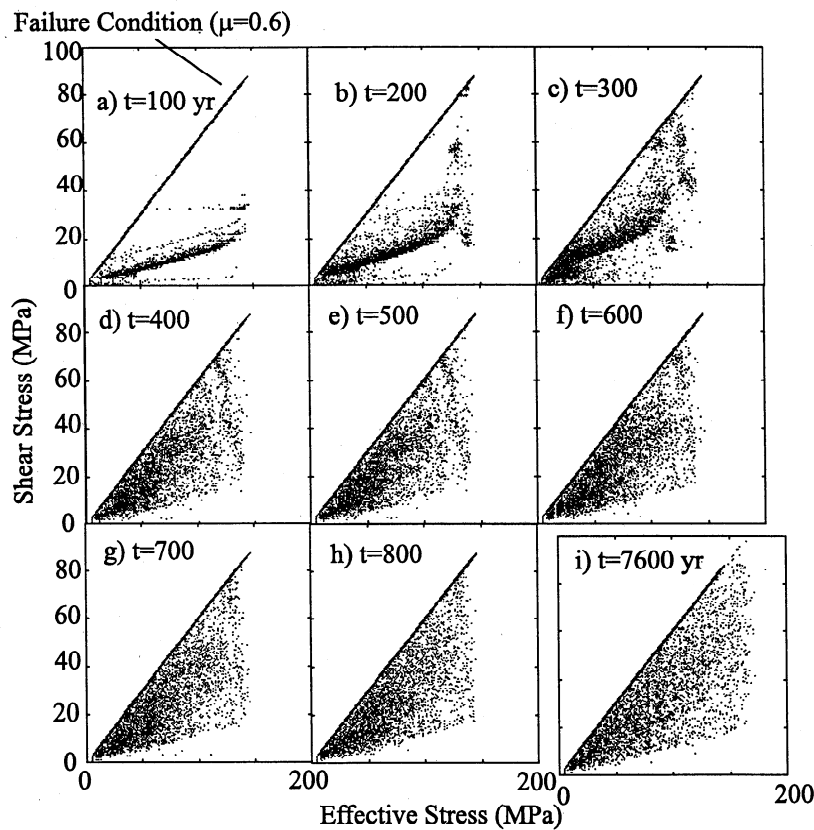


Figure 3. The stress state in Mohr space at different times. The stress state is initially uniform but depth dependent. (a)-(c) As the initial fault plane fails, clusters appear in stress space, (d-h) but the system is not self-organized until the entire stress space is occupied. (i) The complex stress state is the equilibrium state in this model, and is maintained indefinitely. Choosing other friction coefficients or stress drop merely limits the available stress space.

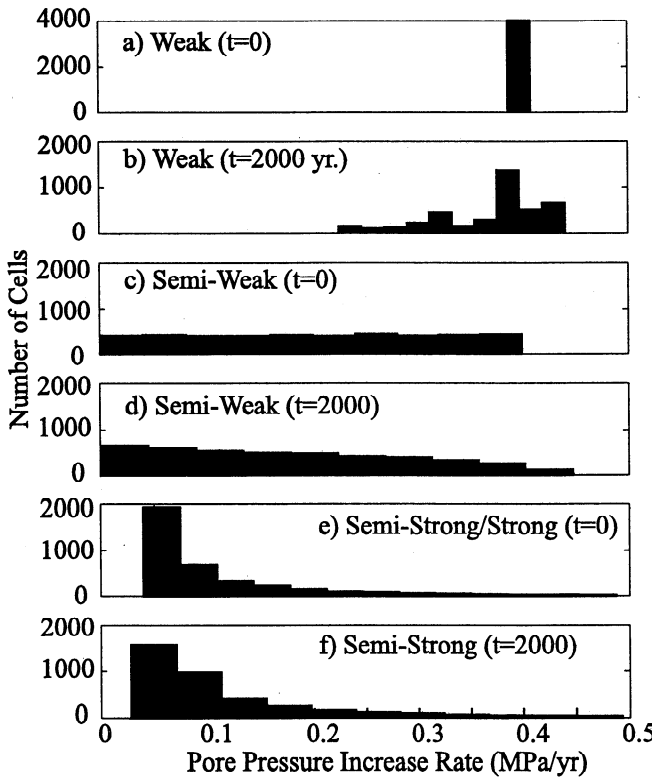


Figure 4. Initial and evolved pore pressure increase rates for the four cases considered. These cases are labeled according to the equilibrium pore pressure state within the fault zone as weak, semiweak, semistrong, and strong. For the weak case the pore pressure increase rates were (a) everywhere the same along the fault, (c) uniformly distributed along the fault, or (e) log-normally distributed along the fault. (b, d, and f) The evolved pore pressure increase rates are shown to demonstrate the pore pressure buildup rates are an evolutionary parameter because of the dependence of the pore pressure increase rate on porosity.

of potential fault zone overpressures. In case 1 all cells in the fault zone were assigned initial pore pressure increase rates of 0.4 MPa/yr (Figure 4a). In case 2 an equal number of cells were assigned pore pressure increase rates ranging from 0.004 to 0.4 MPa/yr (Figure 4c). In case 3, the pore pressure increase rates were log-normally distributed with a range from 0.04 to 4 MPa/yr, heavily weighted toward the lower value (Figure 4c). Case 4 was the same as case 3, except the pore pressure term was “turned off” after 450 years to simulate the effect of stopping fault compaction [Miller, 1996]. Because of the porosity dependence on pore pressure increase rates (equation 2), these rates are an evolutionary parameter between the competing effects of porosity reduction and porosity production. This is shown by the distribution of the evolved rates at 2000 years (Figures 4b, 4d, and 4f).

Rationale for the initial rates is based on assumptions regarding the source to storage capacity ratio in equation (2). Following Segall and Rice [1995], who used experimental results from David *et al.* [1994], pore compressibility is in the range $1 \times 10^{-3} \text{ MPa}^{-1} < \beta_\phi < 1 \times 10^{-2} \text{ MPa}^{-1}$. The lower value applies to porous sandstone, while the upper value is for crystalline rock with crack-like porosity. In our analysis the compressibility term is constrained to $1 \times 10^{-4} \text{ MPa}^{-1} < \beta_\phi < 1 \times 10^{-2} \text{ MPa}^{-1}$, and we assume an initial porosity of 0.05. Assumed values for the source

term are in the range $6 \times 10^{-15} \text{ s}^{-1} < \dot{\Gamma} - \dot{\phi} < 6 \times 10^{-13} \text{ s}^{-1}$. This term approximates potential mechanisms for increasing pore pressure due to fault compaction, plastic pore closure, pressure solution, and fluid sources from prograde metamorphism possibly acting within and/or below fault zones. It will be shown that the general behavior of the model does not depend on these rates, but the steady state fault strength and asperity geometry are dependent on the magnitude of the rates.

4.3. Evolution of Pore Pressures (λ) and Porosity (ϕ)

The controlling parameter in this model is the ratio of pore pressure increase versus shear stress accumulation. Dilatancy is proportional to slip and is therefore implicitly dependent on shear stress accumulation. If fluid pressures increase faster than dilatancy can reduce them, the fault zone evolves to an overpressured, weak fault (case 1). If dilatancy outruns fluid pressure increases, the fault evolves to a normally pressured, strong fault (case 4). Intermediate conditions (cases 2 and 3) are also possible. We loosely define the four cases as weak, semiweak, semistrong, and strong, based on the different steady-state pore pressure conditions achieved. A comparison of the four cases considered (Figure 5) shows the pore pressure condition of one cell located at the center of the matrix ($x=85 \text{ km}$, $z=-8.5 \text{ km}$). These records show the complex fluid pressure path of a computational cell, with spikes indicative of slip-induced hydraulic connectivity with the surrounding permeability network and the overall trend showing the general evolution of the system. The increase in λ at early times reflects the initial condition that the fault is locked, so only the increasing pore pressure mechanisms are operating while dilatant slip is suppressed. Once the original patch has given way (discussed in section 4.4) and the fault accommodates slip along with the plate, both the pore pressure increase and the dilatant slip mechanisms are operating. The result at late time is dynamic pore pressure equilibrium, superimposed with transient spikes associated with the creation and destruction of permeable pathways.

The evolution of fault zone overpressure everywhere along the fault plane is shown (Plate 1) by values of λ at different times for the four cases considered. The evolutionary development of overpressures within the fault zone results from the complex interplay between porosity reduction, slip, porosity production, shear stress, effective stress, and transient permeability networks established and destroyed through time. As already pointed out, following such complexity on the local scale is difficult. However, some global patterns emerge that are consistent in each of the cases and relate to the depth dependence of frictional sliding and the manner of fault slip.

The evolving pore pressure state depends to some extent on the available stress space within which to maneuver. The stress space is limited at shallow depths and much less limited at the deeper locations. Consequently, high pore pressure zones initially develop at shallow depths (e.g., 100 years), which then propagate downward (e.g. 100-300 years). The development of high shear stress concentration along the top and bottom model boundaries causes the initial fault configuration to fail from the outside in, with the concomitant effects on porosity production. The result is that the long-term fault zone overpressures occupy the central portion of the fault plane (around 7-12 km in these cases). Homogenization of the pore pressure state seen at the later times (e.g. 400-600 years) results from the establishment of larger permeability networks as the size of events increases (e.g. the number of cells involved in any one event). As the fault further

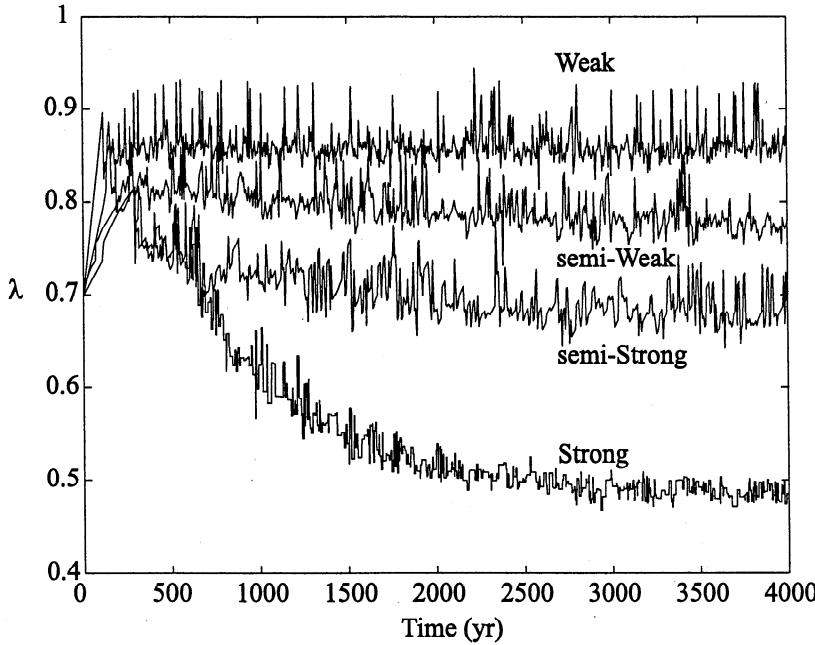


Figure 5. Pore pressure history of one cell located at the center of the computational matrix ($x=85$ km and $z=-8.5$ km) for the different cases considered. The pore pressure history for each of the cases shows that the system evolves to an equilibrium pore pressure state at late time but the individual pore pressure state of a cell is highly complex and reflects the slip-induced hydraulic connectivity to other fluid pressure regimes along the fault plane. The different cases are labeled according to the “equilibrium” pore pressure state achieved at late times.

evolves over the next 4000 years, the overall pore pressure is reduced slightly, but the competition between porosity reduction and porosity production leads to a dynamic equilibrium giving a stable global state of fluid pressure. In that regime, fluid pressures of cells experience random fluctuations (Figure 5) since local regions of high pore pressures continue to develop, dissipate, and migrate within the fault zone.

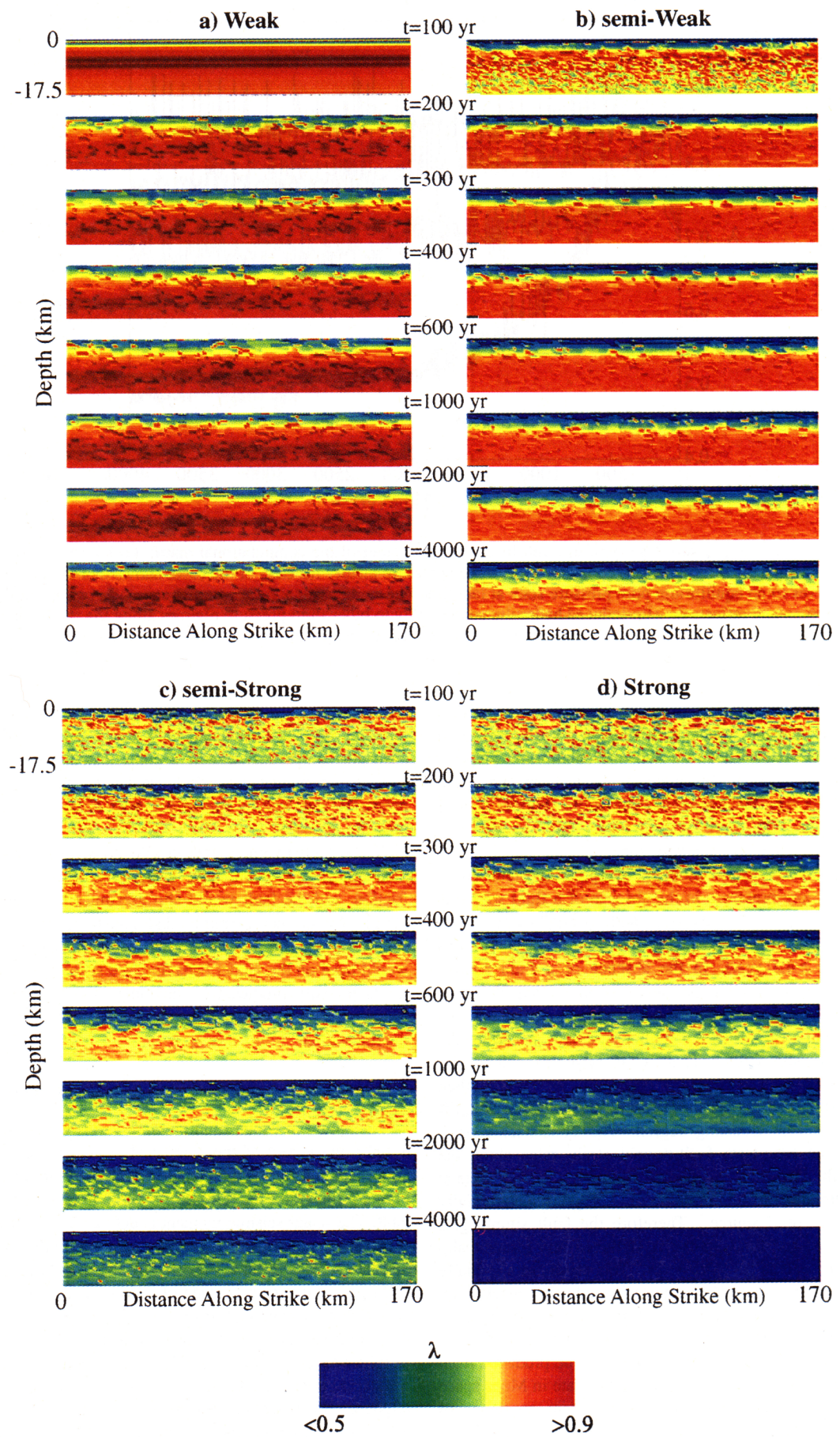
A clear illustration of how modeled overpressured fault zones can deteriorate pore pressures in the absence of a fluid source is given by comparing the “semistrong” and “strong” cases, which differ only in that in the latter case, the fluid source term was turned-off at $t \geq 450$ years. In the absence of a fluid source, dilatancy dominates and high pore pressures are eroded. This case demonstrates the argument of Miller [1996] as to why thrust faulting adjacent to a strike-slip fault can delay an earthquake along the strike-slip fault. That is, if far-field fault-normal displacements tend to compact a strike-slip fault zone, then adjacent thrusting can deflect those displacements through uplift and afterslip in the thrusting region. The consequence is a reduction in the long-term fault-normal strain rates along the strike-slip fault. Reduced fault-normal strain rates limit the rate at which pore pressures can increase due to compaction, essentially shutting off the fluid source. Therefore the fault simply gets stronger because the fluid source is removed and dilatant slip deteriorates any excess pore pressures. This results in a spatially stronger fault than is seen when a porosity reduction mechanism is maintained. An equilibrium fluid pressure is nevertheless achieved in the long term because of the fluid that remains in the system and the limit of how much porosity can be produced from dilatant slip (equation 3). The complex stress state in Mohr space is maintained, and the same dynamical system continues to operate. According to the model then, unless a persisting mechanism for increasing pore pressure exists, dilatant slip will

deteriorate any excess pore pressures, and the fault will evolve to a strong, normally pressured fault zone. The variations in fault (strength) properties suggest a complicated lifetime for a fault zone, a lifetime that can include weakening through elevated pore pressures, followed by strengthening as dilatant slip outruns pore pressure increases.

If the high overpressures developed in the weak fault were maintained, this would have a significant stabilizing effect on friction, and the fault would slip aseismically [Segall and Rice, 1995]. We do not currently distinguish between unstable and stable sliding, and it is not known what effect such a distinction would have on the model behavior. We suspect that aseismic slip limits porosity produced by dilatancy, so once overpressure is achieved, the fault zone would preferentially remain overpressured.

4.4. Moment Accumulation, Moment Release, and Seismicity

The nature in which fluid pressure varies within the fault zone is only one aspect of the dynamical system path. The other is how shear stress is accumulated and released through slip events. Figure 6 illustrates the release of seismic moment from the model fault. The scalar seismic moment is defined as $M_s = GA\delta$, where G is the shear modulus (30 GPa) and A is the fault area slipping a distance δ . Each event is triggered by slip of only one hypocenter, so large events are a cascade of failure propagating through the computational matrix. The seismicity time line shows a random and steady increase in the size of events for the first 300 years and is followed by fluctuations marked by upper and lower limits. This change in character will be shown later to correlate with the ongoing self-organization of the slip deficit along the fault. That is, the final asperity (the last unslipped patch) breaks at around 300 years and is followed by the emergence and destruction of



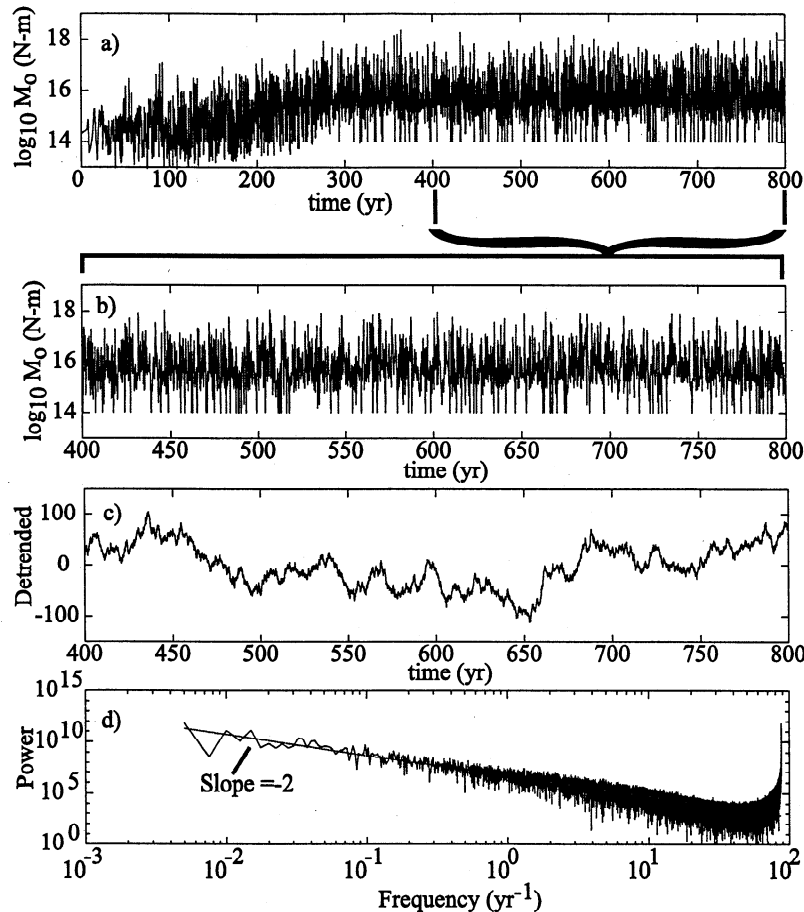


Figure 6. (a) Typical seismicity time line shows a random and steady increase in moment up to about 300 years, which is shown in Plate 2 to relate to failure of the initial fault plane. This record corresponds to the “semistrong” case with a computational matrix of 256x64 cells. The seismicity changes character when the final asperity evolved in the model fails. (b) The timeline from 400–800 years is quantified by (c) taking the FFT of the detrended signal and (d) measuring the power spectrum. The random walk in Figure 6c is shown to be white noise. White noise seismicity signals are found to be independent of the initial input and are a general behavior of this model.

new asperities and slip deficit patterns. The random character of the time line is quantified by measuring its power spectrum. The power spectrum was calculated for the signal from 400 to 800 years (Figure 6b), by detrending the integrated seismic moment (e.g., deviations from a constant moment release). The resulting signal (Figure 6c) has a $1/f^2$ power spectrum (Figure 6d). Thus the seismicity time line in Figure 6b is characterized by f^0 (white noise). These noise attributes of model seismicity remain for the duration of the simulations and are independent of the state of fault zone fluid pressure.

The different cases can be compared directly by looking at the integral of the time series, or moment release, for the duration of the signal. The moment release curve (Figure 7a), shows the time history of the total seismic moment stored along the fault plane, with the reference dashed line showing the seismic moment accumulation from plate motion. The difference between accumulated and released seismic moment is the seismic potential (Figure 7b). Figures 7a and 7b show that the long-term moment release rate and seismic potential are approximately constant after the self-organizational phase and are dependent on the fault

Plate 1. (opposite) Snapshots of the pore pressure state at different times for each of the cases considered. High pore pressure regions initially propagate from the top down because of increasing mean stress, and tend to concentrate at the middle levels at late times. The differences in each case result from the competing effects of porosity reduction and porosity production. (a) In case I, porosity reduction outruns porosity production, so the fault evolves to a highly overpressured, weak fault. (b)-(c) As the fault becomes progressively stronger, porosity production from slip along the boundaries limits pore pressure increases and high pore pressures concentrate at the middle levels. Pore pressures up to 1000 years continue to increase because accumulated slip deficits limit slip-induced porosity production. At late times, dilatant slip begins to deteriorate some of the high pore pressures, but eventually an equilibrium condition is achieved. (d) When the porosity reduction mechanism is switched off, dilatancy dominates and the fault evolves to a strong fault.

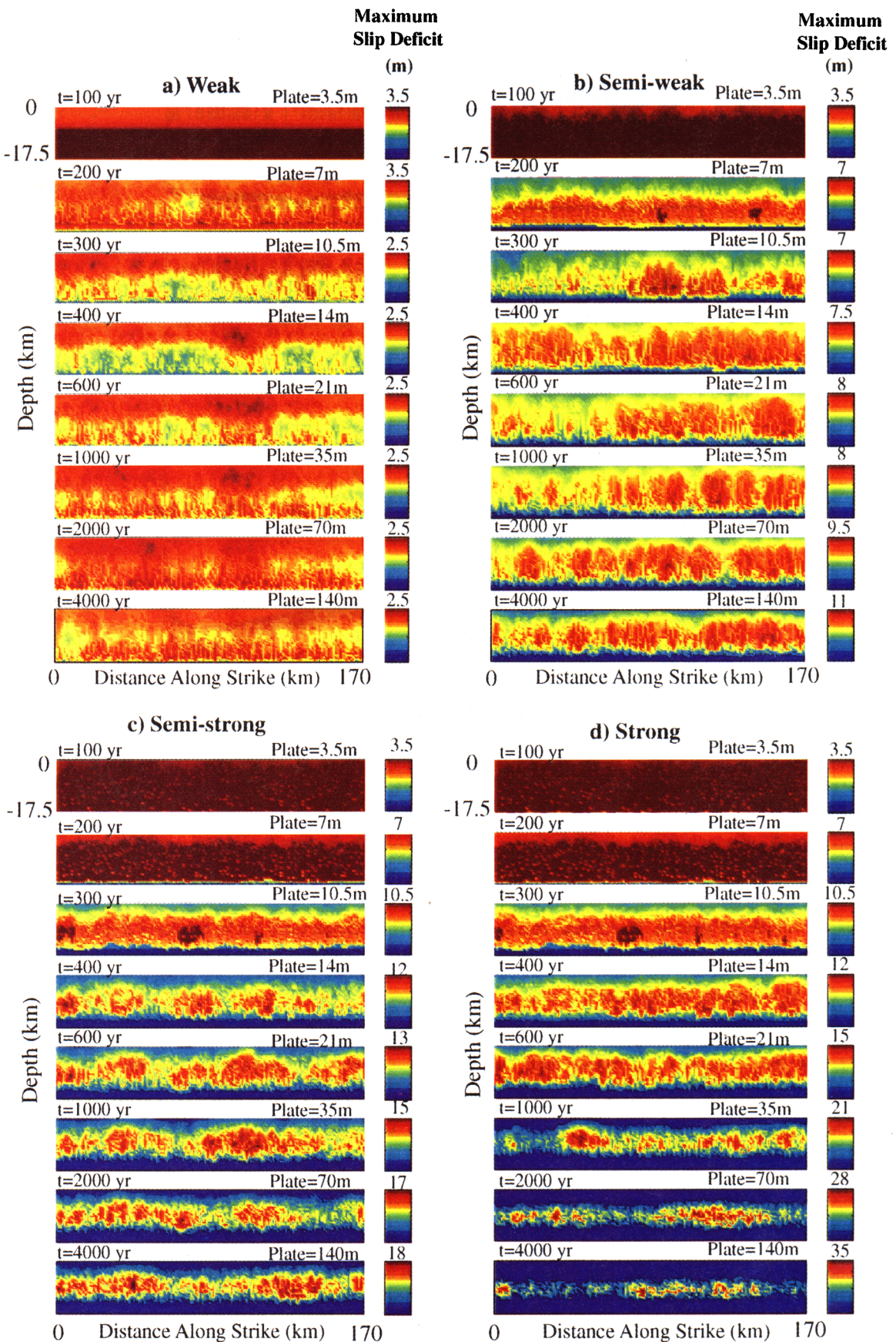


Plate 2. Snapshots of slip-deficit accumulation for the different cases considered. The scale bar to the right of the snapshots shows the maximum 3 m of slip deficits along the fault to highlight the evolved asperity geometry for the different cases and to show maximum slip deficits that accumulate. See text for additional details.

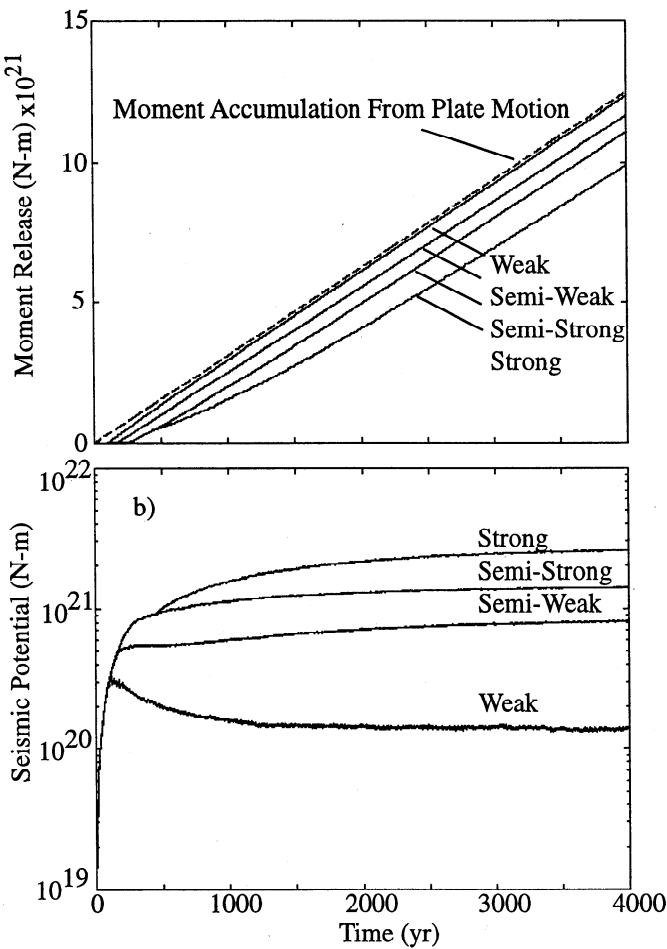


Figure 7. Comparison of the (a) moment release and (b) seismic potential of the different cases considered. The dashed line in Figure 7a is the moment accumulation from plate motion. The model shows different levels of seismic potential that depend on the fault strength. The moment release rates for all cases are relatively constant after the steady state pore pressure state is achieved. See text for additional details.

strength. Stronger faults can simply accumulate larger slip deficits. In the case of stopping fault compaction the moment release rate is reduced temporarily, so the fault becomes stronger and eventually fails as a strong fault. Despite the apparent smoothness of the curves, seismic moment is released in bursts, as is implied by the complexity of the seismicity timeline (Figure 6).

4.5. Long-Term Slip (Deficit) Behavior

The character of the seismicity time line can be understood by visualizing how the fault plane fails (Plate 2). To keep the results on the same scale, we show snapshots of the maximum 3 m of slip deficit accumulated along the fault plane. For example, if the maximum slip deficit along the fault at the time of a snapshot is 18 m, then the color scale has a range from 15–18 m, and slip deficits below 15 m are shown in blue. The slip deficit is the difference between the plate position and cumulative slip at each computational cell. Notice that the total range of slip deficits depends on fault strength, from about 3 m for the weak fault, to about 35 m for the strong fault. The fault is initially locked, so the slip deficit at early times is near the plate displacement along

large regions of the fault. As the fault self-organizes through a sequence of failures, slip deficit concentrates onto patches that have not yet failed.

The failure of the initial fault plane is shown merely for completeness to show how the fault attains an equilibrium slip deficit. Failure of the initial fault plane is not intended to portray the behavior of real faults. The fault plane fails initially from the top and bottom boundaries because of the low effective normal stress and stress concentrations at the base, respectively. In the case of the weak fault (Plate 2a), the entire fault has slipped by 200 years, while portions of the fault plane remain unslipped after 300 years for the progressively stronger faults (Plates 2b–2d).

After the initial failures the fault begins to catch up with the plate as fluid pressures increase and the fault cannot maintain the derived slip deficits. A decrease in seismic potential (Figure 7b) is observed until steady state arises whereby the fault equilibrates to slip deficits of the order of a couple of meters. The evolving slip deficit pattern (e.g., 300–4000 years) shows that the maximum slip deficit concentrates on the upper and lower boundaries, while the central portion sustains varying degrees of intermediate slip deficits. The shallow and deep regions have increased strength because of reduced fluid pressures through dilatant slip, while the central portion slips more readily because of the excess pore pressures shown in Plate 1. In other words, slip at the boundary edges produces porosity, the increased porosity reduces pore pressures, and reduced pore pressures give the upper and lower boundaries higher strength due to increased effective stress. In this case, increases in pore pressure along the fault plane dominate porosity production, and this slip-deficit state is maintained as the system reaches a steady state of porosity reduction and production.

As the fault plane becomes stronger (Plates 2b–2d), the slip-deficit patterns begin to change character. Parts of the initial fault plane remain unslipped for around 300 years. This is marked by a maximum slip deficit occurring between 5 and 15 km (Plate 2b at 300 years). After the entire fault plane has slipped (between 200 and 300 years), asperities are seen to emerge (300 years), disintegrate (400–600 years), and migrate along the fault. The maximum slip deficit is related to the state of the fluid pressure in the fault zone. Up to around 1000 years, the maximum slip deficit is around 7–8 m (Plate 2b), but as dilatancy begins to overcome pore pressure increases, slip deficit grows to around 11 m at 4000 years. The asperity development in this case is more diffuse and occupies a large region of the fault plane because pore pressure production is sufficient to limit the effects of dilatant slip and therefore to limit the accumulation of large slip deficits.

With increasing fault strength (Plates 2c–2d), slip deficits become more concentrated toward the center of the fault plane. Notice at 300 years that the slip deficit of around 10 m is equal to the plate displacement but then fails during the next 100-year interval (e.g., 400 years). The self-organization is complete around 350 years, when the final unslipped patch breaks. After 400 years the slip deficit (asperities) migrates along the fault, showing a nonperiodic buildup and release. Low effective normal stress at the surface and stress concentrations at the base limit the amount of slip deficits that can accumulate along these edges. Meanwhile, fault zone fluid pressures are insufficient to aid failure of the fault plane, causing significant slip deficits to accumulate. A good example of how the initial fault fails is seen in the sequence from 100 to 300 years. At 300 years the final patch of the original fault is on the verge of slipping. Failure of this patch marks the beginning of the self-organized state to which the model arrives and at which it is maintained (refer also

to Figure 3c and 6a). After 300 years, asperities are still observed but change in space and time. The semistrong model reaches an equilibrium slip deficit of around 18 m, increasing to more than 30 m if the pore pressure increase mechanism is removed. According to this model the plate is always dragging the fault along, and the fault maintains (varying) slip deficits throughout its lifetime.

4.6. Comparison of Evolved Mohr-Space Stress States

The different cases examined have some characteristics peculiar to the specifics of the model input, but the overall statistical behavior of the system is independent of that input. The evolved stress state in Mohr space for the different cases (Figure 8) shows that regardless of whether the fault is strong, weak, or in between, the model drifts toward the maximum disorder in the stress state that is available. For the weak fault case the stress state is concentrated near low effective stress, thus limiting the maximum shear stress that can accumulate. In the strong fault case the stress space is extended, but the entire stress space is still occupied.

The extent of the stress space also influences the range of available seismic moment and stress drops. For example, the maximum local stress drop for the weak fault case is around 50 MPa, compared to about 120 MPa for the strong fault case. Notice that some cells (and not always the same cells) reside near failure. If these cells are spatially uncorrelated, then isolated events will result. If on the other hand, the incipient failure is among cells that are spatially correlated, then large events may result giving rise to the seismic scaling relationships that emerge.

4.7. Scaling Relationships

Scaling relationships between the seismic moment, source dimension, and stress drop have been the subject of substantial debate and uncertainty in seismology, and have broad

implications on seismic source physics [Scholz, 1982, 1990; Romanowicz and Rundle, 1993; Okal and Romanowicz, 1994; Scholz, 1994; Abercrombie, 1995]. Compilations of seismic studies show that, in general, the seismic moment M_o scales with the source dimension (L) as $M_o \propto L^3$ along isolines of stress drop. Such a relationship is consistent with theoretical models where the rupture area grows in both length and width ($L-W$), and the stress drop is constant over a scale length that depends on the geometry of the rupture. For a circular crack of radius a the stress drop can be calculated as [Kanamori and Anderson, 1975]

$$\Delta\sigma = \frac{7M_o}{16a^3} \quad (5)$$

where $\Delta\sigma$ is the stress drop and a is the source dimension (with units L). The scalar seismic moment is determined by the zero frequency amplitude of the seismic spectra, and is a reasonably robust measurement. The source dimension is estimated from the extent of aftershocks, from the length of the surface rupture, or from the corner frequency of seismic spectra [Brune, 1970; Madariaga, 1976]. In contrast to the seismic moment, the source dimension is not as well constrained. The range of stress drops is highly variable, from 0.1–100 MPa, with most stress drops between 0.03–30 MPa [Scholz, 1990]. Recently, it has been suggested that cubic self-similar scaling extends to small events with source dimension of about 10 m [Abercrombie, 1995].

In the following discussion, the source dimension (with units L) is defined as \sqrt{A} , where A is the total area of rupture along the model fault plane. Ruptures can be continuous or can jump across regions with no slip and continue again. In this model, stress drop is constant across one computational cell but can vary over the rupture area because of the highly heterogeneous stress-state that exists. Therefore, scaling relationships are not obvious from the outset, but we can search for relationships because the average stress drop ($\bar{\Delta\sigma}$) and rupture area A are computed

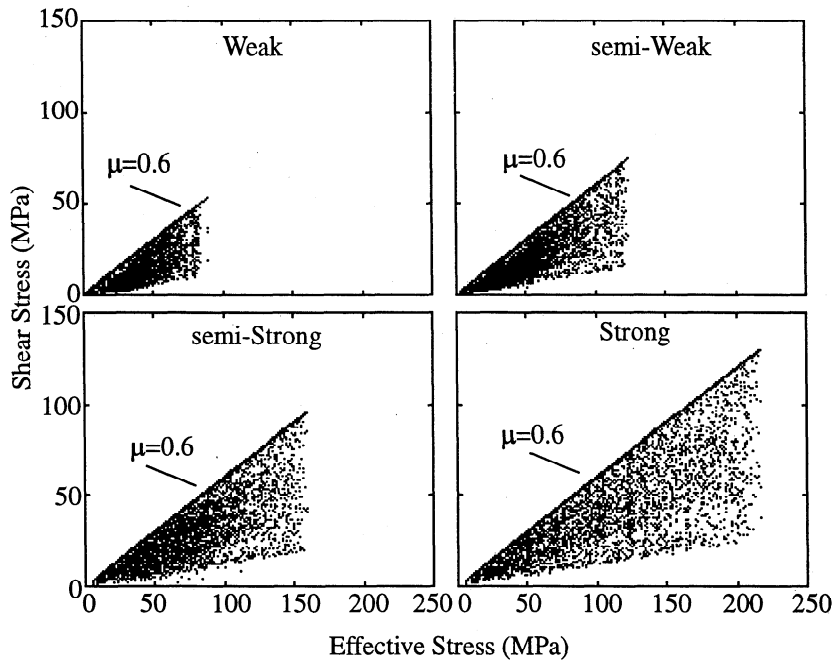


Figure 8. Evolved stress state at 2000 years for the different cases. The general stress state in Mohr space is shown to be independent of the fault strength, but the spatial extent of the stress state is dependent on fault strength.

directly. Since $M_o = GA\delta$ by definition, where the average slip $\bar{\delta} \propto A\bar{\sigma}$, then $M_o \propto A\bar{\sigma}$ for all events. If the average stress drop does not depend on the size of the slipped area (or source dimension), then $M_o \propto L^2$ along isolines of constant stress drop. On the other hand, if stress drop depends on the source dimension (i.e., $\Delta\sigma \propto L$), then $M_o \propto L^3$. Both of these scaling relationships emerge from the model, and can be separated into events that breach the surface and events that are confined at depth.

Plate 3 shows the relationship between seismic moment and source dimension, and Plate 4 shows the relationship of stress drop to moment (Plates 4a-4d), and stress drop to source dimension (Plate 4e-4h). For events that breach the surface (shown in red in Plate 3), the average stress drop scales linearly with the depth extent of the rupture $\Delta\bar{\sigma} \propto z$, so $M_o \propto L^3$. Stress drop scales with the depth extent of the rupture because the average stress drop for all the failing cells is the roughly the "center of mass" of the stress space (Figure 8). This is also seen in Plates 4e-4h, where stress drop for events that reach the surface is shown roughly to scale linearly with the source dimension. For confined events the stress drop depends on the depth of the rupture, but does not scale with the rupture dimension (Plates 4e-4h). Since stress drop does not scale with size, $M_o \propto L^2$. Both scales exist and persist while the system is in the self-organized state. As shown in Figure Plates 3a-3d, the distinction between the two scales depends on the degree of fault weakness. That is, the border between the scales becomes less distinct with increasing fault strength. Notice, however, that all events have average stress drops that fall within the 0.1-100 MPa range typically shown in such a plot [Abercrombie, 1995].

The relationships between seismic moment and stress drop and source dimension and stress drop (Plates 4a-4h) show no clear scaling. Instead, they produce two distinct clusters. The cluster of stress drops for larger events converge to an average stress drop that shows a weak dependency on source dimension. In all cases, the dependencies on stress drop converge to relations with an approximately constant stress drop at large magnitudes. The stress drop at large magnitudes depends on fault strength, and the average stress drop of large ruptures is constrained by the extent of the stress space. This is demonstrated by the histogram of stress drops, and how hypocenters of large model events are related to depth for the different cases (Figures 9a-9b). In the self-organized state and for events that breach the surface, it is found for all cases considered that $M_o \propto L^3$ crossing isolines of stress drop, $\Delta\sigma \propto L$, which implies $\Delta\sigma \propto M_o^{1/3}$.

4.8. Frequency-Size Statistics

The b-value of earthquakes is defined as the slope of the frequency-magnitude relationship

$$\log N = a - bM \quad (6a)$$

where N is the cumulative number of earthquakes above a certain magnitude (M), a is a rate constant, and b describes the decay with size. The b value of regional tectonic earthquakes is claimed to be a universal constant of 1, independent of location [Frohlich and Davis, 1993], and about 1.2-1.5 for volcanic seismicity. This has been used to argue for the self-similarity of earthquakes, but recent studies have shown that the b value changes in both space and time, and for earthquake swarms, b values can range from 0.5 to 1.5 [Turcotte, 1992; Wiemer and Benoit, 1996]. The most common quoted b value is 1 [Scholz, 1990; Okal and Romanowicz, 1994].

Kagan [1994] pointed out that a gamma distribution gives a

better mathematical and physical measure for frequency-size statistics of earthquakes, since it combines (6a) with a gradual cutoff of events having the maximum seismic moment M_o^{\max} that can be produced in the study region. Data from a variety of catalogs corresponding to different seismogenic zones are fit by

$$\varphi(M_o) = C^{-1} M_o^{-1-\beta} \exp(-M_o/M_o^{\max}) \quad (6b)$$

where M_o is the scalar seismic moment, $\beta = (2/3)b$, and C is a normalizing coefficient. M_o^{\max} for shallow seismicity ranges from about 1.0×10^{21} Nm to 1.4×10^{22} Nm. The cumulative frequency-size statistics for this model (Figure 10) are best fit by

$$\varphi(M_o) = C^{-1} M_o^{-0.5} \exp(-6M_o/M_o^{\max}) \quad (7)$$

where M_o^{\max} is determined from the model seismicity catalog. This gives approximate power law statistics for events with $M_o < 5 \cdot 10^{17}$ Nm with a b value of about 0.8. Ben-Zion and Rice [1995] generated similar statistics for cases with prescribed fault zone heterogeneity having a wide range of size scales. Here heterogeneity is not prescribed but rather is generated dynamically by evolving pore pressures in the system. The coefficient in the exponential decay of (7) indicates larger curvature than typical seismicity catalogs, and the curvature depends on the window chosen. We attribute this difference to the lack of very large events that can be generated by this noninertial and simple friction model. The β coefficient (and therefore b value) does not depend on the window chosen.

5. Discussion and Conclusions

Evidence from a variety of sources suggests that high-pressure fluids play an important role in the mechanics of faulting and earthquakes, particularly in relation to fault weakness. Complex seismic behavior, manifested in power laws and other forms of broad earthquake statistics, indicate that earthquakes and faulting are heterogeneous, high-dimensional dynamical systems. We have presented a model that attempts to reconcile both of these constraints on an earthquake fault by using high pore pressures and shear stress changes as the controls on the dynamic evolution of the system.

The model is simple in physics but rich in behavior. The investigation of a wide range of possible input parameters demonstrated that the system evolves to a general "attractor" that is independent of those parameters. The state to which this model develops, and maintains, is the highest degree of stress state disorder along the fault plane. The heterogeneous stress state translates to asperity development along the fault, and the strength of these asperities is determined by the fluid pressure distribution. If the fault zone is highly overpressured, the fault can only sustain slip deficits of the order of a few meters. In contrast, at lower fluid pressures, slip deficits on the order of tens of meters can be developed and maintained. Since the ongoing deep plate velocity continuously loads the fault plane, slip-deficit accumulation depends on the maximum shear stress that can be sustained. This, in turn, is limited by the friction failure condition and the state of the effective normal stress.

An important result from this study is that high fluid pressures are not in themselves necessary to generate complexity. Rather, it is the mere presence of fluids in the fault zone and the coupling of the fluids with the evolving deformation. The chain of events that set up the complex stress state in Mohr space, even for homogeneous initial fluid pressures and compaction rates, is as

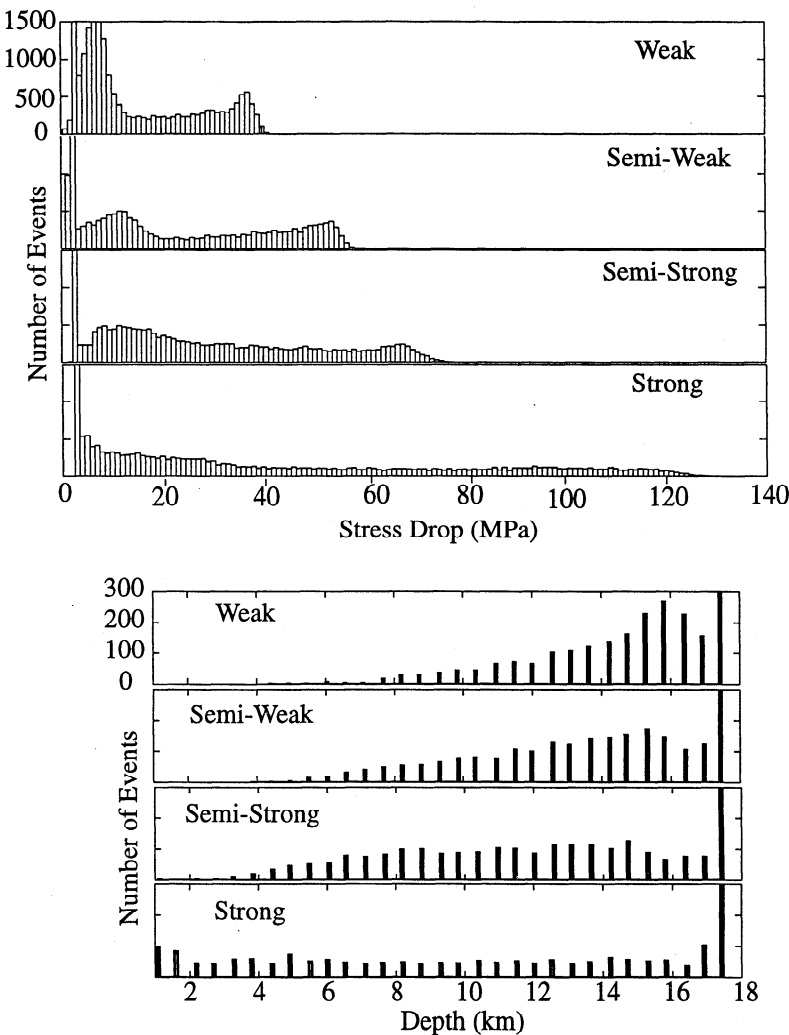


Figure 9. Comparisons of (a) stress drop histograms and (b) hypocentral depths for the four cases. The histograms are for events greater than the mean value of seismic moment for the model earthquake catalog investigated and represent about 4000 events.

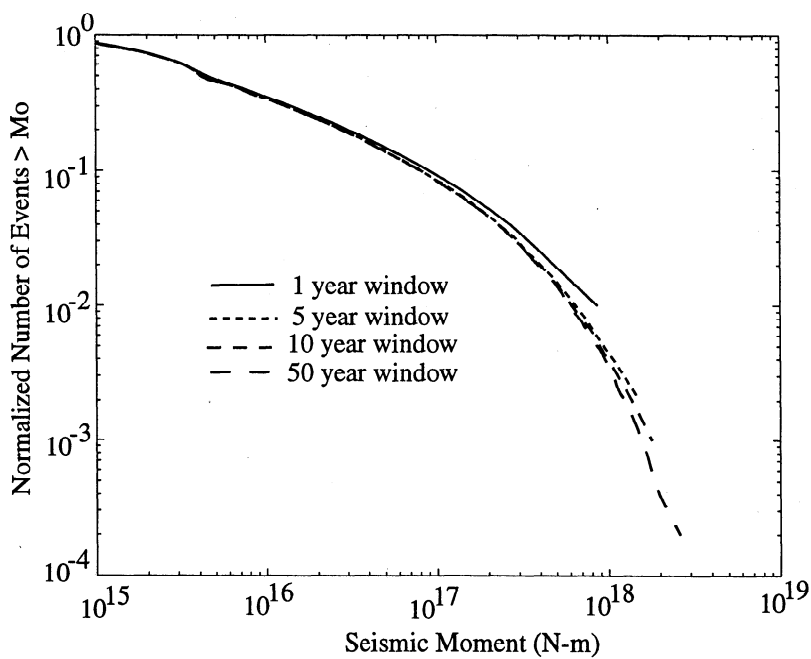


Figure 10. Frequency-size statistics evaluated for different time windows. These data are best fit to a gamma distribution with $\beta \sim 0.5$ ($b \sim 0.8$).

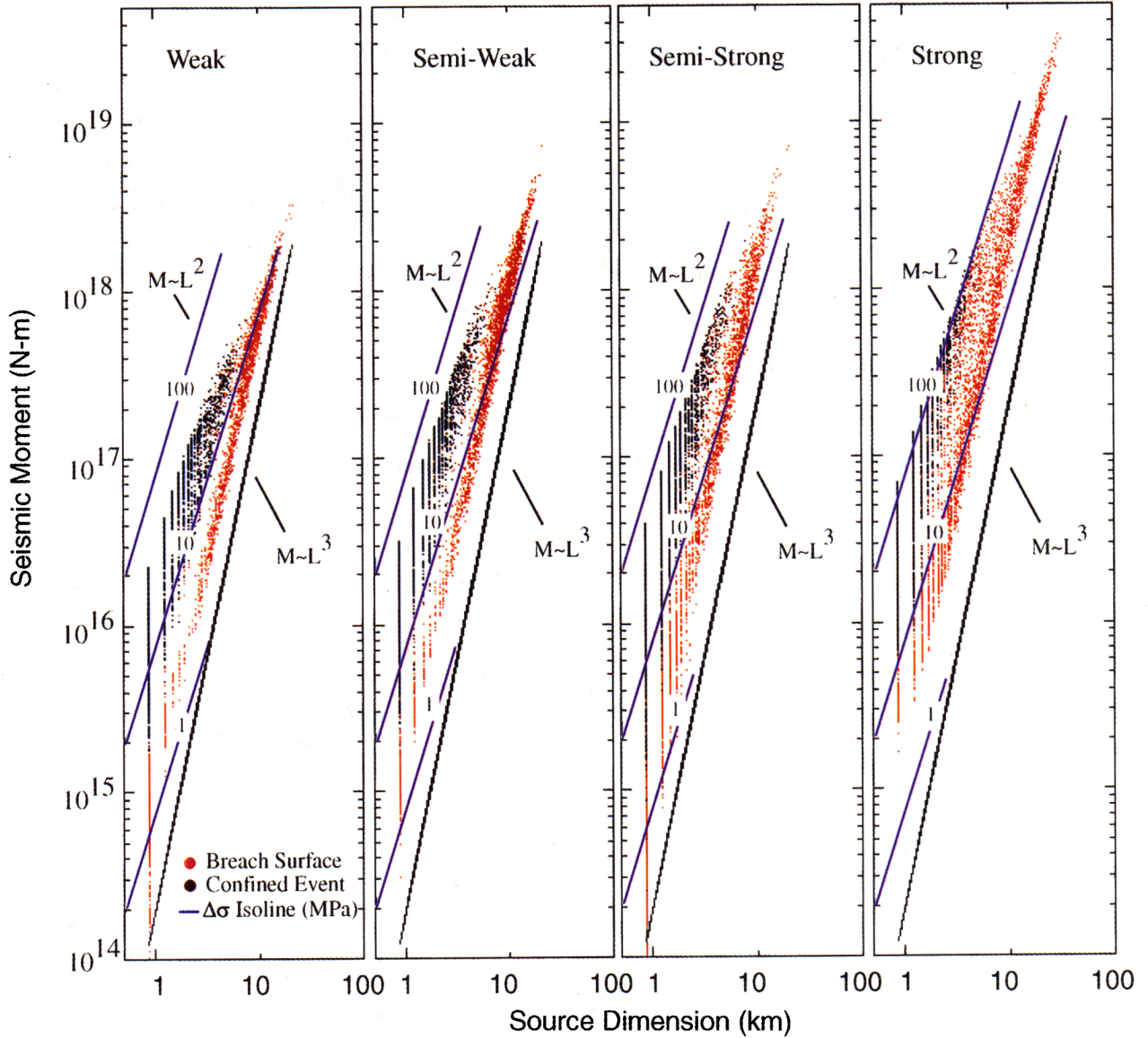


Plate 3. Evolved moment-source dimension relationships for 10,000 events from the model catalog showing that both scales $M_o \propto L^3$ and $M_o \propto L^2$ exist and persist in the model. Red points represent events that breach the surface, and stress drop isolines are shown in blue.

follows. For a fault that is initially locked, stress concentrations at the upper and lower boundaries lead to slip events that include the creation of new porosity. This new porosity perturbs the uniform fluid pressure state, setting in motion a feedback mechanism that allows the stress path to change in both the shear stress and the effective normal stress directions.

This model produces complex fluid pressure variations, stress states, and slip distributions along the fault, leading to the simple global statistical result of filling the available Mohr space. The analogy of evolution toward maximum entropy is clearly manifested in the behavior of this model. The complexity in Mohr-space results in a state that can include stress drops in any range, from low stress drops for many failing cells to high stress drops for individually failing cells. Mixed-mode stress drops also arise, as the failure processes involve cells in a variety of stress states. Seismic moment is released as white noise, while the long-term moment release rate can be approximated as a constant.

This is true whether the fault is weak, semiweak, semistrong or strong. Long-term moment release rates evolve approximately to a constant; independent of fault strength, once the system has reached equilibrium-disordered state. Although the average moment release rate is constant, the seismic potential of the system depends on fault weakness.

Asperity development in the model has broad implications for the seismic process. An asperity is defined as that part of the fault that is stuck and the part of the fault that produces high moment release in large rupture. Typically, asperities are assumed to occur because of geometric variations along strike. Here we show that asperities can also occur on a planar fault as a consequence of stress state variations along strike brought on by the dynamic interplay of shear stress and effective normal stress. These Mohr-space asperities evolve in space and time and produce spatiotemporal variations of slip deficit along the fault plane. Any subsequent event must rupture across this heterogeneous

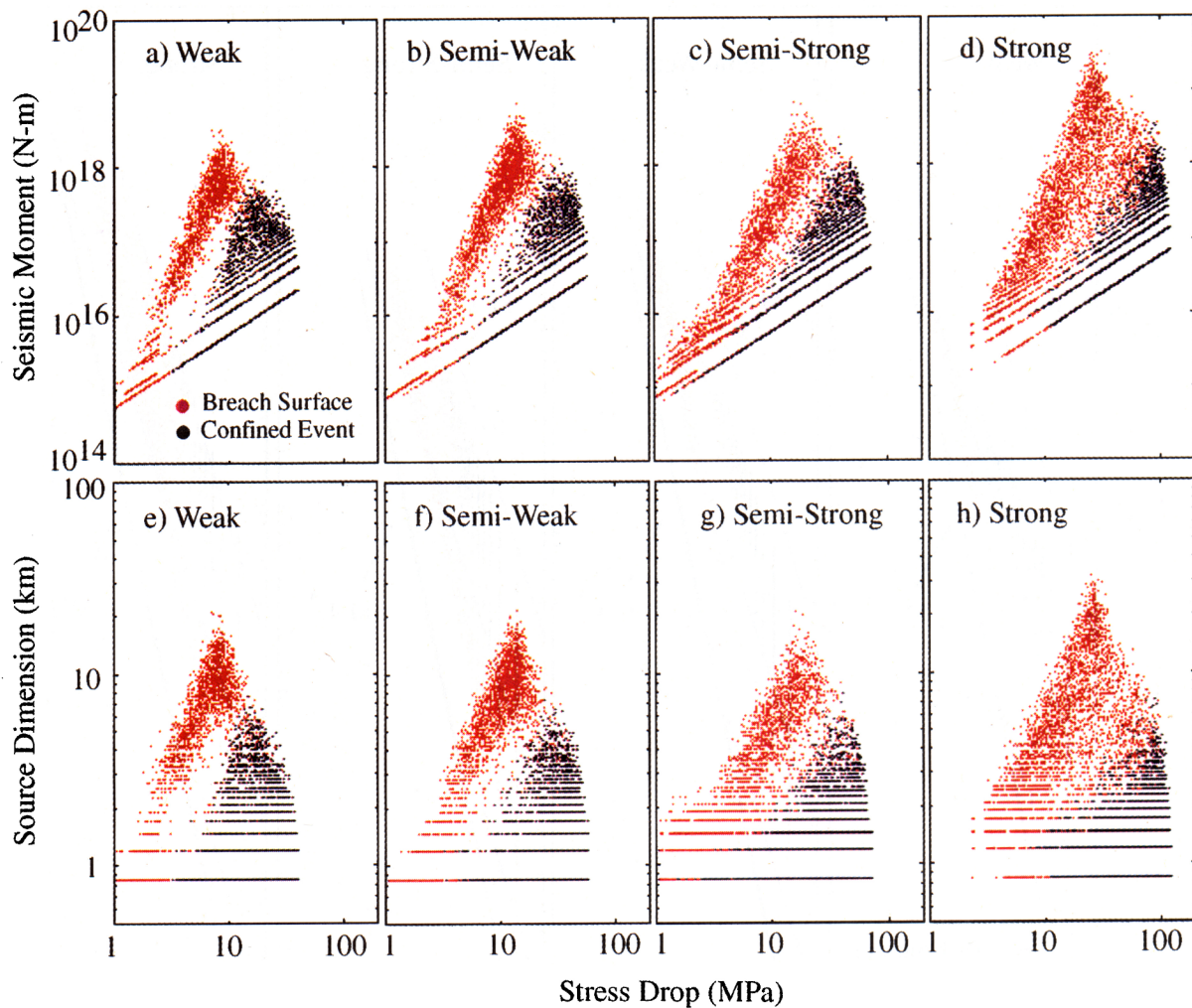


Plate 4. Evolved scaling relationships between seismic moment and source dimension with stress drop. Events that breach the surface are shown in red. These relationships show clusters of events that converge to a constant average stress drop, the value of which depends on fault strength.

stress and slip state, thus producing complex rupture patterns. This would be manifested in short rise times, heterogeneous stress drop and variable slip in earthquakes, in direct agreement with conclusions drawn from the 1984 Morgan Hill earthquake in California [Beroza and Mikumo, 1996]. Indeed, if this model captures the dominant processes controlling seismicity, then such variations in earthquake ruptures must always be the case along mature fault zones.

If a fault is overpressured, then it must be continuously supplied with a fluid source if the overpressure is to be maintained. In the absence of a fluid source, porosity created from dilatant slip will eventually erode high pore pressure zones, and the fault will evolve toward a normally pressured (hydrostatic) pore pressure environment. The source of fluid can take the form of a direct fluid source (e.g., dehydration, a fluid source at depth), or from a reduction in the available pore space. In the model described here, we have focused on a source from porosity reduction, primarily via direct fault-normal compaction. This type of fluid source would be expected in transpressional tectonic environments where strain is partitioned such that a significant component of fault normal plate motion occurs.

In the simple model considered here, we have deliberately ignored a number of processes that might be considered for future studies. First, poroelastic effects coupling changes in normal stress to pore pressure changes have not been included. Second, we have ignored coseismic wave propagation effects. We have treated the fault as a plane, thereby restricting fluid flow and fluid pressure variations within this plane. Studies of fault zones reveal structures which indicate a low-permeability fault core surrounded by high-permeability fracture zones and embedded in a low permeability country rock [Caine et al., 1996]. We have ignored processes which allow flow out of the fault core and into the fracture zone, a process described by Sleep [1995] as a leaky fault. Damage and permeability enhancement away from the fault core could produce a higher degree of fluid pressure variations along strike, resulting in even more heterogeneity than is currently generated by this model. An analysis of the three-dimensional strain field, to be addressed in a future paper, reveals complex strain invariants along strike that could be used to determine damage evolution and hydraulic properties away from the fault core. Also, the model is currently limited to vertical strike-slip faults but can easily be extended to other fault

orientations and geometry by including the solutions of *Okada* [1992] for other dislocation sources. Incorporating faults of other orientations and multiple fault interactions can be coupled to existing stress transfer models for seismic hazard analysis and for investigating rupture patterns in other tectonic environments.

Acknowledgments. We appreciate the thought-provoking reviews from Ruth Harris, Norm Sleep, and Tom Parsons. Thanks are also extended to Yuri Podladchikov, Ian Main, and Chris Scholz for numerous discussions, and to Bill Stuart for kindly providing portions of his elastic dislocation code. This work was funded by a grant from the ETH Research Commission (Project 0-20-857-94).

References

- Abercrombie, R., Earthquake source scaling relationships from -1 to 5 ML using seismograms recorded at 2.5 km depth, *J. Geophys. Res.*, **100**, 24,015-24,036, 1995.
- Bak, P., and C. Tang, Earthquakes as a self-organized critical phenomenon, *J. Geophys. Res.*, **94**, 15,635-15,637, 1989.
- Ben-Zion, Y., and J.R. Rice, Earthquake failure sequences along a cellular fault zone in a three-dimensional elastic solid containing asperity and nonasperity regions, *J. Geophys. Res.*, **98**, 14,109-14,131, 1993.
- Ben-Zion, Y., and J.R. Rice, Slip patterns and earthquake populations along different classes of faults in elastic solids, *J. Geophys. Res.*, **100**, 12,959-12,983, 1995.
- Beroza, G.C., and T. Mikumo, Short slip duration in dynamic rupture in the presence of heterogeneous fault properties, *J. Geophys. Res.*, **101**, 22,449-22,460, 1996.
- Blanpied, M.L., D.A. Lockner, and J.D. Byerlee, An earthquake mechanism based on rapid sealing of faults, *Nature*, **358**, 574-576, 1992.
- Boatwright, J., and M. Cocco, Frictional constraints on crustal faulting, *J. Geophys. Res.*, **101**, 13,895-13,909, 1996.
- Braun, J., and C. Beaumont, Three-dimensional numerical experiments of strain partitioning at oblique plate boundaries: Implications for contrasting tectonic styles in the southern Coast Ranges, California, and central South Island, New Zealand, *J. Geophys. Res.*, **100**, 18,059-18,074, 1995.
- Brune, J., Tectonic stress and the spectra of seismic shear waves from earthquakes, *J. Geophys. Res.*, **75**, 4997-5009, 1970.
- Byerlee, J.D., Friction, overpressure, and fault normal compression, *Geophys. Res. Lett.*, **17**, 2109-2112, 1990.
- Byerlee, J.D., Model for episodic flow of high-pressure water in fault zones before earthquakes, *Geology*, **21**, 303-306, 1993.
- Caine, J.S., J.P. Evans, and C.B. Forster, Fault zone architecture and permeability structure, *Geology*, **24**, 1025-1028, 1996.
- Carlson, J.M., and J.S. Langer, Properties of earthquakes generated by fault dynamics, *Phys. Rev. Lett.*, **62**, 2632-2653, 1989.
- Chinnery, M.A., The stress changes that accompany strike-slip faulting, *Bull. Seismol. Soc. Am.*, **53**, 921-932, 1963.
- Cochard, A., and R. Madariaga, Complexity of seismicity due to highly rate-dependent friction, *J. Geophys. Res.*, **101**, 25,321-25,336, 1996.
- Connolly, J.A.D., Devolatilization-generated fluid pressure and deformation-propagated fluid flow during prograde regional metamorphism, *J. Geophys. Res.*, **102**, 18,149-18,173, 1997.
- Connolly, J.A.D., and Y.Y. Podladchikov, Compaction-driven fluid flow in viscoelastic rock, *Geodin. Acta*, **11**, 55-84, 1998.
- Das, S., and B.V. Kostrov, An investigation of the complexity of the earthquake source time function using dynamic faulting models, *J. Geophys. Res.*, **93**, 8035-8050, 1988.
- David, C., T.-f. Wong, W. Zhu, and J. Zhang, Laboratory measurement of compaction-induced permeability change in porous rocks: implications for the generation and maintenance of pore pressure excess in the crust, *Pure Appl. Geophys.*, **143**, 425-456, 1994.
- Deng, J., and L.R. Sykes, Stress evolution in southern California and triggering of moderate-, small-, and micro-size earthquakes, *J. Geophys. Res.*, **102**, 24,411-24,435, 1997.
- Fisher, A., and G. Zwart, Relation between permeability and effective stress along a plate-boundary fault, Barbados accretionary complex, *Geology*, **24**, 307-310, 1996.
- Frohlich, C., and S.D. Davis, Teleseismic *b* values. Or, much ado about 1.0, *J. Geophys. Res.*, **98**, 631-644, 1993.
- Gavrilenko, P., and Y. Gueguen, Fluid overpressure and pressure solution in the crust, *Tectonophysics*, **217**, 91-110, 1993.
- Harris, R.A., Introduction to the special section: Stress triggers, stress shadows, and implications for seismic hazard, *J. Geophys. Res.*, **103**, 24,347-24,358, 1998.
- Harris, R.A., and P. Segall, Detection of a locked zone at depth on the Parkfield segment of the San Andreas fault, *J. Geophys. Res.*, **92**, 7945-7962, 1987.
- Harris, R.A., and R.W. Simpson, In the Shadow of 1857. The effect of the great Ft. Tejon earthquake on subsequent earthquakes in southern California, *Geophys. Res. Lett.*, **23**, 229-232, 1996.
- Heimpel, M., Critical behavior and the evolution of fault strength during earthquake cycles, *Nature*, **388**, 865-868, 1997.
- Henderson, J.R., and B. Maillot, The influence of fluid flow in fault zones on patterns of seismicity: A numerical investigation, *J. Geophys. Res.*, **102**, 2915-2924, 1997.
- Hickman, S.H., and B. Evans, Kinetics of pressure solution at halite-silica interfaces and intergranular clay films, *J. Geophys. Res.*, **100**, 13113-13132, 1995.
- Hickman, S., R. Sibson, and R. Bruhn, Introduction to special section: Mechanical involvement of fluids and faulting, *J. Geophys. Res.*, **100**, 12831-12840, 1995.
- Kagan, Y.Y., Observational evidence for earthquakes as a nonlinear dynamic process, *Physica D*, **77**, 160-192, 1994.
- Kanamori, H., and D. Anderson, Theoretical basis of some empirical relations in seismology, *Bull. Seismol. Soc. Am.*, **65**, 1073-1095, 1975.
- King, G.C.P., R.S. Stein, and J. Lin, Static stress changes and the triggering of earthquakes, *Bull. Seismol. Soc. Am.*, **84**, 935-953, 1994.
- Lachenbruch, A.H., and J.H. Sass, Heat flow and energetics of the San Andreas fault zone, *J. Geophys. Res.*, **85**, 6185-6223, 1980.
- Lockner, D.A., and J.D. Byerlee, Dilatancy in hydraulically isolated faults and the suppression of instability, *Geophys. Res. Lett.*, **21**, 2353-2356, 1994.
- Lockner, D.A., and J.D. Byerlee, An earthquake instability model based on faults containing high fluid-pressure compartments, *Pure Appl. Geophys.*, **145**, 717-745, 1995.
- Madariaga, R., Dynamics of an expanding circular fault, *Bull. Seismol. Soc. Am.*, **66**, 636-666, 1976.
- Main, I., Statistical physics, seismogenesis, and seismic hazard, *Rev. Geophys.*, **34**, 433-462, 1996.
- Marone, C., C.B. Raleigh, and C.H. Scholz, Frictional behavior and constitutive modeling of simulated fault gouge, *J. Geophys. Res.*, **95**, 7007-7025, 1990.
- Miller, S.A., Fluid-mediated influence of adjacent thrusting on the seismic cycle at Parkfield, *Nature*, **382**, 799-802, 1996.
- Miller, S.A., The behavior of a 3-dimensional fluid-controlled earthquake model: Applications and implications, Ph.D. thesis, 123pp., ETH, Zürich, 1997.
- Miller, S.A., A. Nur, and D.L. Olgaard, Earthquakes as a coupled shear stress-high pore pressure dynamical system, *Geophys. Res. Lett.*, **23**, 197-200, 1996.
- Moore, J.C., et al., Abnormal fluid pressures and fault-zone dilation in the Barbados accretionary prism: Evidence from logging while drilling, *Geology*, **23**, 605-608, 1995.
- Nur, A., Nonuniform friction as a basis for earthquake mechanics, *Pure Appl. Geophys.*, **116**, 964-989, 1978.
- Okada, Y., Internal deformation due to shear and tensile faults in a half-space, *Bull. Seismol. Soc. Am.*, **82**, 1018-1040, 1992.
- Okal, E.A., and B.A. Romanowicz, On the variation of *b*-values with earthquake size, *Phys. Earth Planet. Inter.*, **87**, 55-76, 1994.
- Reasenberg, P.A., and R.W. Simpson, Response of regional seismicity to static stress change produced by the Loma Prieta earthquake, *Science*, **255**, 1687-1690, 1992.
- Rice, J.R., Fault stress states, pore pressure redistributions, and the weakness of the San Andreas fault, in *Fault Mechanics and Transport Properties of Rocks*, edited by B. Evans and T.-F. Wong, pp. 476-503, Academic, San Diego, Calif., 1992.
- Rice, J.R., Spatio-temporal complexity of slip on a fault, *J. Geophys. Res.*, **98**, 9885-9907, 1993.
- Robinson, R., and R. Benites, Synthetic seismicity models of multiple interacting faults, *J. Geophys. Res.*, **100**, 18,229-18,238, 1995.
- Romanowicz, B., and J.B. Rundle, On scaling relations for large earthquakes, *Bull. Seismol. Soc. Am.*, **83**, 1294-1297, 1993.
- Sass, J.H., C.F. Williams, A.H. Lachenbruch, S.P. Galanis, and F.V. Grubb, Thermal regime of the San Andreas fault near Parkfield, California, *J. Geophys. Res.*, **103**, 27,575-27,585, 1998.

- Scholz, C.H., Scaling laws for large earthquakes: Consequences for physical models, *Bull. Seismol. Soc. Am.*, 72, 1-14, 1982.
- Scholz, C.H., *The Mechanics of Earthquakes and Faulting*, Cambridge Univ. Press, New York, 1990.
- Scholz, C.H., A reappraisal of large earthquake scaling, *Bull. Seismol. Soc. Am.*, 84, 215-218, 1994.
- Segall, P., and J.R. Rice, Dilatancy, compaction, and slip instability of a fluid infiltrated fault, *J. Geophys. Res.*, 100, 22,155-22,171, 1995.
- Shaw, B.E., Model quakes in the two-dimensional wave equation, *J. Geophys. Res.*, 102, 27,367-27,377, 1997.
- Sibson, R.H., Interactions between temperature and pore fluid pressure during an earthquake faulting and a mechanism for partial or total stress relief, *Nature*, 243, 66-68, 1973.
- Sibson, R.H., Fault-valve behavior and the hydrostatic-lithostatic fluid pressure interface, *Earth Sci. Rev.*, 32, 141-144, 1992.
- Sleep, N.H., Ductile creep, compaction, and rate and state dependent friction within major fault zones, *J. Geophys. Res.*, 100, 13,065-13,080, 1995.
- Sleep, N.H., and M.L. Blanpied, Creep, compaction and the weak rheology of major faults, *Nature*, 359, 687-692, 1992.
- Stein, R.S., and G. Ekström, Seismicity and geometry of a 110-km-long blind thrust fault. 2. Synthesis of the 1982-1985 California earthquake sequence, *J. Geophys. Res.*, 97, 4865-4883, 1992.
- Stein, R.S., A.B. Aykut, and J.H. Dieterich, Progressive failure on the North Anatolian fault zone since 1939 by earthquake stress triggering, *Geophys. J. Int.*, 128, 594-604, 1997.
- Stuart, W.D., Forecast model for large and great earthquakes in southern California, *J. Geophys. Res.*, 91, 13771-13786, 1986.
- Stuart, W.D., R.J. Archuleta, and A.G. Lindh, Forecast model for moderate earthquakes near Parkfield, California, *J. Geophys. Res.*, 90, 592-604, 1985.
- Turcotte, D.L., *Fractals and Chaos in Geology and Geodynamics*, 221 pp., Cambridge Univ. Press, New York, 1992.
- Walder, J., and A. Nur, Porosity reduction and pore pressure development, *J. Geophys. Res.*, 89, 11,539-11,548, 1984.
- Wallace, R.E., The San Andreas fault system California, U.S. Geol. Surv., Prof. Pap. 1515, 1990.
- Wiemer, S., and J.P. Benoit, Mapping the *b*-value anomaly at 100 km depth in the Alaska and New Zealand subduction zones, *Geophys. Res. Lett.*, 23, 1577-1580, 1996.
- Wong, T.-f., S.-C. Ko, and D.L. Olgaard, Generation and maintenance of pore pressure excess in a dehydrating system, 2, Theoretical analysis, *J. Geophys. Res.*, 102, 841-852, 1997.
- Yamashita, T., Simulation of seismicity due to fluid migration in a fault zone, *Geophys. J. Int.*, 132, 674-686, 1998.
- Zhong, S., and M. Gurnis, Interaction of weak faults and non-Newtonian rheology produces plate tectonics in a 3D model of mantle flow, *Nature*, 383, 245-248, 1996.
- Zoback, M.D., and G.C. Beroza, Evidence for near-frictionless faulting in the 1989 (*M* 6.9) Loma Prieta, California, earthquake and its aftershocks, *Geology*, 21, 181-185, 1993.
- Zoback, M.D., et. al., New evidence on the state of stress on the San Andreas fault system, *Science*, 238, 1105-1111, 1987.

Y. Ben-Zion, Department of Earth Sciences, University of Southern California, Los Angeles CA 90089-0740. (benzion@topaz.ucs.edu)

J. P. Burg, Geology Institute, Sonneggstr. 5, ETH-Zurich, 8092 Zurich, Switzerland. (jpb@erdw.ethz.ch)

S. A. Miller, Geology Institute, HIL D22.3, ETH-Zurich, 8093 Zurich Switzerland. (steve@erdw.ethz.ch)

(Received June 1, 1998; revised October 19, 1998; accepted November 4, 1998.)